First-principles study of elastic and phonon properties of the heavy fermion compound CeMg

2009 J. Phys.: Condens. Matter 21 246001

(http://iopscience.iop.org/0953-8984/21/24/246001)

J. Phys.: Condens. Matter **21** (2009) 246001 (12pp) doi:10.1088/0953-8984/21/24/246001

First-principles study of elastic and phonon properties of the heavy fermion compound CeMg

S L Shang[1], L G Hector Jr[2], Y Wang[1], H Zhang[1] and Z K Liu[1]

[1] Department of Materials Science and Engineering, The Pennsylvania State University, University Park, PA 16802, USA
[2] Materials and Processes Laboratory, General Motors Research and Development Center, Warren, MI 48090, USA

E-mail: sus26@psu.edu (S L Shang)

Received 25 February 2009, in final form 23 April 2009
Published 21 May 2009
Online at stacks.iop.org/JPhysCM/21/246001

Abstract

Elasticity tensor components, C_{ij}, the crystallographic dependence of Poisson's ratio, the phase stability, and vibrational spectra are computed for nonmagnetic and magnetic CeMg (1:1 Ce:Mg) structures using density functional theory. Results from both the generalized gradient approximation (GGA), and the GGA + U, based upon an effective on-site Coulomb potential, U_{eff}, are investigated. The GGA low energy structure, with wavevector along [110], disagrees with experiment, while the [100] structure from experiment is predicted as the 0 K structure in the GGA + U. Accurate estimation of the 20 K Néel temperature can only be achieved with small U_{eff}, which suggests that CeMg is not a strongly correlated system. For all CeMg structures investigated, we find $C_{11} \approx C_{44}$; this is consistent with the near equivalency of transverse and longitudinal sound speeds. The origin of this behavior is the negative stretching force constants for the interaction between the second- and third-nearest-neighbor Mg and Ce ions, respectively. Results are compared with neutron scattering experiments at 30 and 110 K.

(Some figures in this article are in colour only in the electronic version)

1. Introduction

Cerium-based heavy fermion compounds constitute a scientifically interesting class of materials that have attracted substantial interest due to their intriguing properties and technological significance. For example, pressure-induced superconductivity has been reported in $CeIn_3$, $CePd_2Si_2$, $CeCu_2Ge_2$, and $CeRhIn_5$ [1]. Anomalies in magnetic susceptibility and heat capacity at low temperatures [2–4] involving the Kondo effect and the Ruderman–Kittel–Kasuya–Yosida (RKKY) interaction have also been reported [5, 6]. Cerium serves a crucial role in Mg alloys which are the focus of current worldwide interest as potential alternatives to heavier Al and steel alloys in automotive structures. Cerium, as part of mish metals (which are mixtures of rare earth (RE) elements, e.g., 51.7% Ce, 23.1% La, 18.6%, Nd, and 6.5% Pr, in mass %) [7], is often added to improve Mg alloy formability and enhance corrosion resistance. Despite the fact that Ce has very limited solubility in Mg, various Ce-containing precipitates in Mg alloys have been identified [8–13]. Cerium additions have been shown to affect Mg alloy texture leading to improved ductility [14]. The mechanisms by which Ce additions and Ce–Mg precipitates lead to reported improvements in Mg alloys are complex and poorly understood. Moreover, fundamental property information for Ce–Mg compounds, such as elastic and vibrational properties, is scarce.

An important component of the Ce–Mg phase diagram is paramagnetic (PM) CeMg (1:1 Ce:Mg) which has the cubic CsCl-type structure at room temperature ($a \approx 3.9$ Å [15], metallic) and shows Kondo-type behavior [3]. Below the $T_N \sim 20$ K [4, 16] Néel temperature, CeMg orders antiferromagnetically (AFM) with a strong tetragonal distortion [17]. Pierre *et al* [18] measured the phonon dispersion relations of the PM structure of CeMg at 30 K and 110 K with neutron scattering experiments and estimated the elastic constants of CeMg from acoustic phonon branches.

Their phonon dispersion results show no significant differences at the temperatures associated with the measurements. Using the implementation of plane wave density functional theory (DFT) in the VASP code [19, 20], Wu and Hu [21] computed the elasticity tensor components, C_{ij}, of nonmagnetic (NM) CeMg and found qualitative accord with the Pierre *et al* [18] estimates from 110 K measurements. A special Ce potential ($5s^2 5p^6 5d 6s^2$ valence) within the generalized gradient approximation (PW91) [22] based on the projector-augmented wave (PAW) method [23] was used. Here, f electrons are not treated explicitly but are kept frozen in the core. This special potential is problematic, however, since it leads to the erroneous conclusion that low temperature magnetic CeMg structures are nonmagnetic (NM) states even at higher volumes (greater than the equilibrium structures).

Many Ce-based heavy fermion compounds exhibit anomalies in the C_{ij} temperature behavior and in other thermodynamic properties such as the specific heat, magnetic susceptibility and resistivity [24]. For the majority of crystalline materials, C_{44} is less than C_{11}, for which v_t is less than v_ℓ, where v_t and v_ℓ are transverse and longitudinal sound speeds, respectively [25]. For some materials, C_{44} has been found to be nearly equal to (or even exceed) C_{11}, which suggests an elastic anomaly since v_ℓ is comparable to (or less than) v_t. For example, $C_{11} = 8.1$ and $C_{44} = 10.1$ GPa for BCC Ba [26]. This is related to the hybridization of free electron states with d bands close to the Fermi level [26]. However, the possibility of an f state system with different magnetic states (such as CeMg) exhibiting this behavior has not been extensively investigated. None of the existing studies of CeMg, including that of Wu and Hu [21], suggests elastic anomalies which are associated with the relative slopes of acoustic zone center phonon dispersion branches from which v_t and v_ℓ can be computed. Interestingly, the C_{ij} from experiment [18] and calculation [21] suggest a negative Poisson's ratio for elongation along [110] measured in $[1\bar{1}0]$ (i.e. the lateral direction) [27].

In this paper, we examine the phase stability of nonmagnetic (NM), ferromagnetic (FM), and antiferromagnetic (AFM) CeMg structures with first-principles density functional theory (DFT) within the generalized gradient approximation (GGA). For comparison with the GGA predictions, ancillary calculations using the GGA + U method, in which an effective on-site Coulomb potential for the f states is added to the GGA, were also conducted (the dynamical mean field approach [28] could also be applied to CeMg as an alternative to the GGA + U). The two methods are found to lead to different conclusions about the 0 K structure of CeMg. We examine each structure for $C_{11} \approx C_{44}$. For this purpose, and to facilitate comparisons with experiments, components of the elasticity tensor, C_{ij}, and vibrational spectra based upon the direct method for lattice dynamics were computed for each CeMg structure using VASP [19, 20] as the computational engine. The origin of the CeMg elastic behavior is revealed through examination of the relative sizes of the force constants for the interaction between nearest neighbor ions computed from the phonon calculations. Finally, we look for negative values of Poisson's ratio for elongation along [110] measured in $[1\bar{1}0]$ following [27].

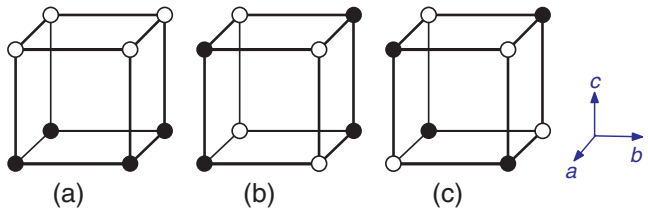

Figure 1. Positions and spin alignments of Ce ions in the AFM CeMg structures with the CsCl-type structure. ●: Ce+ (spin up), ○: Ce− (spin down). (a) AFM100, (b) AFM110, (c) AFM111. Additional structural details are listed in table 1.

The remainder of this paper is organized as follows. Section 2 details the NM, FM, and AFM CeMg structures examined in this paper. Our computational approach is described in section 3. Predicted structural properties, phase stability and choice of the effective U value (U_{eff}) for the GGA + U are considered in section 4, while section 5 describes our C_{ij} calculations for each CeMg structure and explores Poisson's ratio along specific crystallographic directions. Section 6 details our phonon calculations (mainly by using the GGA) and addresses the origin of the intriguing elastic behavior in terms of force constants from our phonon calculations. Major results of the paper are summarized in section 7.

2. CeMg structures

Space groups, lattice vectors, and Wyckoff positions for the five CeMg structures investigated herein are detailed in table 1. The three CeMg AFM structures are such that the Ce ions (spin up Ce+ or spin down Ce−) reside in planes that are perpendicular to the [001] direction (AFM100), the [110] direction (AFM110), and the [111] direction (AFM111). Figure 1 shows spin alignments of the Ce ions in representative cubic cells with the solid circles representing Ce+ (spin up) and the open circles denoting Ce− (spin down). A $P4/mmm$ tetragonal space group is associated with the spin orderings in AFM100 (figure 1(a)) and AFM110 (figure 1(b)), while AFM111 (figure 1(c)) is cubic with $Fm\bar{3}m$. The AFM structures can also be distinguished by the positions of the second-nearest neighbors (2nn) surrounding the Ce+ (or Ce−) ions. In AFM100, there are two Ce− ions along the c-axis direction and four Ce+ ions along the a-axis (and b-axis) directions surrounding one Ce+ ion. Note that the a- and b-axes are equivalent for each tetragonal structure. In AFM110, there are four Ce− ions along the a-axis (and b-axis) directions and two Ce+ ions along the c-axis direction surrounding one Ce+ ion. In AFM111, there are six Ce− ions surrounding one Ce+ ion. Magnetic CeMg structures containing more than four ions (not considered here) can be generated by mixing the FM, AFM100, AFM110, and AFM111 structures.

3. Computational approach

All calculations in this study are based on the implementation of plane wave density functional theory (DFT) in the Vienna

Table 1. Space groups, lattice vectors, and Wyckoff positions of Ce (including spin up, Ce+, and spin down, Ce−) and Mg for NM, FM, and AFM CeMg structures. In AFM100, AFM110, and AFM111, the two independent Ce ions (Ce+ and Ce−) are antiferromagnetic along [001], [110], and [111], respectively (see figure 1). Here, the ideal c/a ratio is set as unity, 1, for the tetragonal structures in order to compare their distortions relative to the cubic structure.

			Wyckoff position		
State	Space group	Lattice vector	Ce or (Ce+)	Ce−	Mg
NM	$Pm\bar{3}m$	$\begin{pmatrix} a & 0 & 0 \\ 0 & a & 0 \\ 0 & 0 & a \end{pmatrix}$	1a (0, 0, 0)		1b (1/2, 1/2, 1/2)
FM	$Pm\bar{3}m$	$\begin{pmatrix} a & 0 & 0 \\ 0 & a & 0 \\ 0 & 0 & a \end{pmatrix}$	1a (0, 0, 0)		1b (1/2, 1/2, 1/2)
AFM100	$P4/mmm$	$\begin{pmatrix} a & 0 & 0 \\ 0 & a & 0 \\ 0 & 0 & 2c \end{pmatrix}$	1a (0,0,0)	1b (0, 0, 1/2)	2h (1/2, 1/2, z) $z = 1/4$ [a]
AFM110	$P4/mmm$	$\begin{pmatrix} a & a & 0 \\ -a & a & 0 \\ 0 & 0 & c \end{pmatrix}$	1a (0,0,0)	1c (1/2, 1/2, 0)	2e (0, 1/2, 1/2)
AFM111	$Fm\bar{3}m$	$\begin{pmatrix} 0 & a & a \\ a & 0 & a \\ a & a & 0 \end{pmatrix}$	4a (0, 0, 0)	4b (1/2, 1/2, 1/2)	8c (1/4, 1/4, 1/4)

[a] The ideal value.

ab initio simulation package (VASP) [19, 20]. The electron–ion interactions are described by the full potential projector-augmented wave (PAW) method [23], and the exchange–correlation is treated within the GGA of Perdew–Burke–Ernzerhof (PBE) [29] in conjunction with the interpolation formula of Vosko *et al* [30]. The PAW potential set comprised a $5s^2 5p^6 4f 5d 6s^2$ valence configuration for Ce and $2p^6 3s^2$ for Mg. We also accounted for on-site Coulomb repulsion among localized Ce 4f electrons in ancillary calculations based upon the implementation of the GGA + U method of Dudarev *et al* [31] in VASP. This method requires that an effective Coulomb interaction, $U_{\text{eff}} = U - J$, be specified. Here, U is the strong on-site Coulomb interaction due to the energy increase from an electron addition to the Ce 4f states, and J is the screened exchange energy [32]. It is worth mentioning that the GGA + U method as implemented in VASP introduces magnetism. Its application to nonmagnetic structures is to be avoided since it will yield non-physical results (e.g. the equilibrium cell volume decreases with increasing U_{eff}). We note that U_{eff} can in fact be computed in a self-consistent way on the basis of the approach of Cococcioni *et al* [33]. For example $U_{\text{eff}} = 2.5$–3.5 eV for LDA + U and $U_{\text{eff}} = 1.5$–2.0 eV for GGA + U were applied for CeO_2 [34]. However, we were able to make a suitable choice for U_{eff}, as has been done in previous work, without the need for additional calculations. We based our choice of the U_{eff} upon two important experimental results that must be predicted with reasonable accuracy for magnetic CeMg structures: (1) the AFM100 ground state of CeMg [17], and (2) the ∼20 K Néel temperature of CeMg [4, 16]. We note that the VASP implementation of the Dudarev *et al* [31] method has been used in studies of the electronic structure and thermodynamic properties of CeO_2, Ce_2O_3, and CeO_{2-x} [35, 36]; optical properties of α- and γ-CeS_2 [37]; molecular adsorption on transition metal oxide surfaces [38]; phase stability of lithium ion battery materials [39, 40]; electric polarization in a $LaMnO_3/BaTiO_3$ superlattice [41]; and point defects in uranium dioxide [42]. As mentioned above, the common approach is to select U_{eff} on the basis of desired experimental properties.

Lattice parameters and single-crystal bulk moduli were computed through a fit to an equation of state [43]. For this purpose, two successive constant volume shape optimizations on each primitive cell were conducted. Total energies on the VASP-optimized structures were calculated by integration over a Monkhorst–Pack [44] mesh of k-points in the Brillouin zone with the linear tetrahedron method including Blöchl corrections [45]. k-point meshes that provided convergence of electronic energies to at least 0.1 meV f.u. (f.u. = formula unit) were utilized along with a 500 eV cutoff energy for all structures. All force components were relaxed to at least 10^{-4} eV Å^{-1}.

The C_{ij} were computed with the optimized primitive cell geometries using the stress-based least-squares fitting method of LePage and Saxe [46]. This method uses the stresses computed in VASP as inputs to a least-squares fit of the unknowns in the linear stress–strain equations for a sequence of symmetry-unique strains. Here the unknowns are the three and six independent elastic constants for cubic and tetragonal symmetries, respectively. The moduli are computed from the first derivatives of the VASP-computed stresses with respect to strain, rather than from the second derivatives of the total energy with respect to strain (e.g., as in [47]). Perhaps the most advantageous aspect of this method is its full exploitation of symmetry which allows for maximum computational efficiency with the VASP. Tests were conducted with selected strains to determine the total number of strains necessary to minimize the least-squares errors for each C_{ij}. It was determined that application of four successive strain values, namely, 0.4%, 0.5%, 0.6%, and 0.7%, was adequate for obtaining $\leqslant 1\%$ statistical error in each C_{ij} for all CeMg structures. The $Pm\bar{3}m$ symmetry required three distortions per strain, leading to two structures with $P4/mmm$ symmetry and one structure with $Cmmm$ symmetry. A total of

thirteen VASP geometry optimizations (three for each of the four selected strains, and the undistorted structure) were required to compute C_{ij}. The same applied for the $Fm\bar{3}m$ space group except that two distorted structures with the $P4/mmm$ symmetry and one with $Immm$ symmetry were required. The $P4/mmm$ structures required six distortions per strain, leading to two $Pmmm$ structures, two $P4/mmm$ structures, one $P2/m$ structure, and one $Cmmm$ structure. Twenty-five VASP geometry optimizations (six for each of the four selected strains and the undistorted structure) were required. The quality of the least-squares fit, as gauged by the computed least-squares residual, was $\leqslant 1\%$ for all C_{ij} calculations. The small residuals indicate that anharmonic effects due to the applied strains in the computed C_{ij} were negligible. Tests with additional strains showed no significant deviation from the results reported here. All C_{ij} computations employed the same DFT convergence criteria as the calculations on the undistorted structures. Previous applications of the least-squares method for calculation of the C_{ij} wherein VASP was used as the computational engine may be found in [48–53].

Vibrational spectra were computed by means of the direct approach [54] (or supercell method [55]) to lattice dynamics in the PHONON code [56] with VASP again the computational engine. The direct method involves construction of $N+1$ supercells: an unperturbed supercell and N perturbed supercells, where N is the number of crystallographically independent displacements of the constituent ions. In each perturbed supercell, a single atom is displaced in a Cartesian direction in such a way that the N supercells explore all of the degrees of freedom of each symmetry-unique atomic site. In this way, the entire Brillouin zone is explored with suitably constructed supercells. Displacements of ± 0.02 Å were applied to the ions (displacements as large as ± 0.03 Å and as small as ± 0.01 Å were found to produce no significant differences from results calculated for the ± 0.02 Å displacements). The supercell size was chosen such that interactions between equivalent ions in periodic images were negligible, as were the computed force constants at the boundaries of each supercell. For all CeMg structures, $2 \times 2 \times 2$ supercells were used. This involved 16 ions/supercell for the NM, FM, and AFM111 structures and 32 ions/supercell for the AFM100 and AFM110 structures. Ancillary phonon calculations with larger supercells revealed no significant differences from results with the $2 \times 2 \times 2$ supercells. Reciprocal space integration was performed by means of the Methfessel–Paxton technique [57] with a smearing width of 0.05 eV (the phonon results showed no sensitivity to smaller deviations in smearing width above and below 0.05 eV). Additional details on the phonon methodology can be found in [50, 58].

4. Structural properties and phase stability

Figure 2(a) shows the GGA-predicted spin magnetic moments of Ce (or the site-projected moments for the AFM structures) with atomic volume for the FM and AFM structures. The spin magnetic moments increase with increasing volume for all magnetic structures, as expected. For the range of atomic volumes shown, the spin moments of the AFM100 and AFM110 are nearly identical. Each is consistently greater than those computed for AFM111. Computed spin moments for the CeMg FM structure fall between those for the AFM structures with volumes ranging from 28.2 to 31 Å^3, achieving peak values at the largest atomic volumes. Extensive tests at volumes below 24 Å^3 revealed that all magnetic states converge to the NM state.

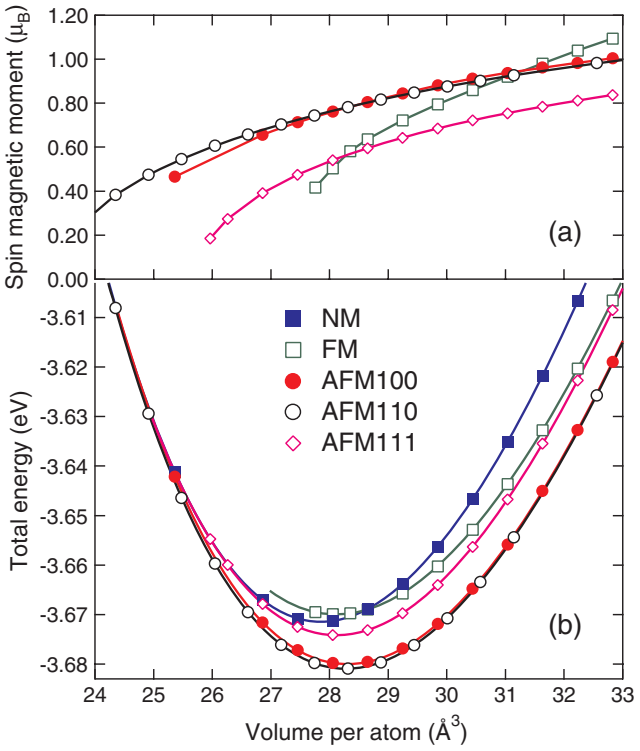

Figure 2. (a) GGA-predicted Ce site-projected spin magnetic moments (μ_B) (only the + value is shown for the AFM structures) and (b) total energy per atom as a function of atomic volume for CeMg structures detailed in table 1.

Figure 2(b) shows the volume-dependent total energies for each CeMg structure from the GGA calculations. The VASP-computed energy–volume points were fit to the following equation of state (EOS) [43]:

$$E(V) = a_0' + b_0' V^{-1/3} + c_0' V^{-2/3} + d_0' V^{-1}, \qquad (1)$$

where V is the volume and a_0', b_0', c_0' and d_0' are fitting parameters. The corresponding equilibrium lattice constants, a, c, cell volumes, V, single-crystal bulk moduli, B, bulk modulus pressure derivatives, B', and spin magnetic moments, MM, estimated on the basis of the EOS fits, are listed in table 2. The equilibrium energy/ion relative to AFM110, which is our predicted low energy structure from the GGA (see figure 2(b)), is tabulated as ΔE. Of the three AFM structures, we find the AFM110 structure to have the lowest GGA-predicted equilibrium energy, with the AFM100 structure only 0.95 meV/ion (i.e., 1.9 meV per magnetic Ce ion) higher in energy (see figure 2(b) and details in table 2). The phase stability of CeMg from the GGA disagrees with the ground state of AFM100 from experiment [17]. We therefore conducted ancillary

Table 2. CeMg properties calculated from the GGA and the GGA + U ($U_{\text{eff}} = 0.4$ eV), together with measured properties of CeMg (see the structural details in table 1), including the lattice parameters a and c (ideal $c/a = 1$; see table 1), volume per ion (V), bulk modulus (B), bulk modulus pressure derivative (B'), and the relative energy per ion (ΔE) with respect to AFM110 estimated by equation of state (EOS) fitting of equation (1). The spin magnetic moment per Ce ion (MM) is also listed.

Structures	a, c (Å)	V (Å^3)	B (GPa)	B'	ΔE (meV)	MM (μ_B)
NM (GGA)	3.819	27.85	37.8	3.64	9.48	
FM (GGA)	3.831	28.12	32.1	3.19	11.01	0.52
FM (GGA + U)	3.830	28.09	33.6	3.41	17.83	0.47
AFM100 (GGA)[a]	3.784, 3.955	28.31	33.8	3.44	0.95	0.78[b]
AFM100 (GGA + U)[a]	3.776, 3.987	28.42	33.9	3.46	−0.30	0.85[b]
AFM110 (GGA)[c]	3.877, 3.763	28.28	34.0	3.59	0.00	0.78[b]
AFM110 (GGA + U)[c]	3.753, 3.888	28.37	34.1	3.51	0.00	0.83[b]
AFM111 (GGA)	3.831	28.12	33.6	3.42	6.79	0.55[b]
AFM111 (GGA + U)	3.837	28.25	34.0	3.39	7.80	0.68[b]
Expt	3.908[d]	29.84[e]	37.8[f]			
	3.898[d]	29.61[e]				
	3.901[d]	29.68[e]				

[a] Relaxed c/a ratios for AFM100:1.045 (GGA) and 1.056 (GGA + U).
[b] Site-projected value.
[c] Relaxed c/a ratios for AFM110:0.971 (GGA) and 0.965 (GGA + U).
[d] Tabulated experimental data for the cubic structure [15].
[e] Calculated values obtained from the experimental data in [15].
[f] Estimated value from the measured phonon dispersion curves at 110 K [18].

calculations with the GGA + U to investigate the effect of the correlated Ce 4f states on the phase stability. Figure 3 shows the equilibrium relative energy of AFM100 with respect to AFM110, $\Delta E[E(\text{AFM100}) - E(\text{AFM110})]$, as a function of the effective Coulomb interaction U_{eff}. When $U_{\text{eff}} > 0.34$ eV, AFM100 becomes the ground state as shown in figure 3. This U_{eff} value was subsequently adjusted by accounting for the measured ∼20 K Néel temperature [4, 16]. Using the energy versus volume curves from the GGA + U with $U_{\text{eff}} > 0.34$ eV, we found that $U_{\text{eff}} = 0.4$ eV results in an estimated CeMg Néel temperature that is very close to 20 K. Our estimated Néel temperature is based upon: (i) the assumption that the PM structure is a mixed spin-flipping configuration (SFC) involving FM and AFM structures (except for AFM100), and (ii) the distributions of AFM100 and SFC at elevated temperatures can be predicted with the partition function method recently detailed in our density functional study of the Ce isostructural phase transition [59]. In fact, on the basis of the partition function method [59], the minimum energy difference between the ground state and the low energy magnetic configuration is found to be roughly proportional to the Néel (or Curie) temperature. With $U_{\text{eff}} = 0.4$ eV for CeMg, the energy of the ground state AFM100 structure is 0.3 meV/ion lower than that of AFM110 (see figure 3 and table 2), which therefore gives us a reasonable prediction of the Néel temperature for CeMg. We noticed that comparably small values of U_{eff} were also used in other studies. For example, Cococcioni [60] and Yang *et al* [61] both used small U_{eff} (<1 eV) in their studies of magnetic transition metals. The small value of U_{eff} used in the present study suggests that CeMg is not strongly correlated and its role may be thought of as nothing more than a small (semi-empirical) correction to the GGA that is required to obtain reasonable agreement with the experimental Néel temperature and to predict the 0 K magnetic structure that is consistent with experiment.

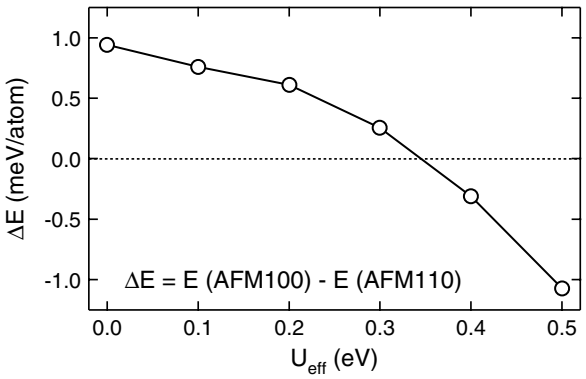

Figure 3. Relative energy ΔE of AFM100 with respective to AFM110 as a function of the effective Coulomb interaction U_{eff}.

The EOS fit properties based on the energy versus volume curves from the GGA + U ($U_{\text{eff}} = 0.4$ eV) are also listed in table 2. In order to probe the influence of U_{eff} and compare with other Ce-containing materials studied with the DFT + U method (see [36] and the references within), large U_{eff} values (e.g. 1.6 eV previously used to predict thermodynamics of the Ce isostructural phase transition [59]) will also be used to investigate the elastic properties of CeMg, although these larger values do not lead to prediction of a reasonable Néel temperature for CeMg.

Regarding the equilibrium lattice parameters (or volumes) of CeMg, table 2 shows that values from both the GGA and the GGA + U ($U_{\text{eff}} = 0.4$ eV) are smaller (∼2%) than the room temperature measurements [15]. Similar observations have been made for other Ce compounds where the VASP Ce

Table 3. Calculation results obtained from least-squares fittings of strain versus stress data points with the GGA and GGA + U ($U_{\text{eff}} = 0.4$ and 1.6 eV) together with measured elastic properties (in GPa) of each CeMg structure (see table 1). A numerical label is listed in the first column of each row to facilitate discussion of the results tabulated herein. Included are elasticity tensor components, C_{ij}, the bulk modulus, B, and shear modulus, G (Hill polycrystalline moduli), the polycrystalline Poisson's ratio ν_{poly}, and the minimum Poisson's ratio ν_{min}. All calculations were conducted at the predicted equilibrium volumes (see table 2 and figure 4). To compare with the least-squares method, the C_{ij} of the NM structure were computed with different methods, namely, phonon and the force constant (FC) ones.

	Structure	C_{11}	C_{33}	C_{12}	C_{13}	C_{44}	C_{66}	B_{Hill}	G_{Hill}	ν_{ploy}	ν_{min}
(1)	NM	47.6		32.0		49.0		37.2	24.2	0.23	−0.46
(2)	NM (phonon)	36.8		31.0		51.8		32.9	19.5	0.25	−0.74
(3)	NM (FC)	36.9		31.2		52.2		33.1	19.5	0.25	−0.74
(4)	FM	37.4		23.9		46.7		28.4	22.3	0.19	−0.50
(5)	AFM100	44.3	38.4	28.9	28.4	45.4	45.7	33.0	21.9	0.23	−0.49
(6)	AFM100 ($U_{\text{eff}} = 0.4$ eV)	48.1	43.2	28.9	30.4	45.0	44.8	35.4	23.1	0.24	−0.45
(7)	AFM100 ($U_{\text{eff}} = 1.6$ eV)	48.2	48.9	25.6	27.2	38.8	37.9	33.9	23.3	0.22	−0.27
(8)	AFM110[a]	80.8	42.2	−10.7	30.2	46.3	7.0	33.7	21.6	0.24	−0.55
(9)	AFM110[b]	42.1	42.2	28.1	30.2	46.3	45.8	33.7	21.6	0.24	−0.55
(10)	AFM111	43.5		28.8		47.7		33.7	23.2	0.22	−0.47
(11)	PM expt.[c]	48.5		32.5		35		37.8	19.5	0.28	−0.30

[a] First-principles values predicted on the basis of the lattice vectors given in table 1.

[b] Transformed values C'_{ij} from a 45° rotation of C_{ij} about the z-axis.

[c] Estimated values from the measured phonon dispersion curves at 110 K on the paramagnetic CsCl-type CeMg [18].

potential with f states in the valence has been applied [37, 62]. Corrections for thermal expansion and the volume dependence of zero-point energy will in fact lead to lattice parameters that are in closer accord with experiment [50]. The c/a ratios predicted from the GGA (GGA+U) for AFM110 and AFM100 are, respectively, 0.971 (0.965) and 1.045 (1.056), while that from experiment is 1.013 [17]. This suggests the possibility that the measurements may have been conducted on a mixture of the AFM100 and AFM110 states due to the small energy difference between them (0.95 and −0.3 meV/ion from the GGA and the GGA + U, respectively; see table 2). We define an ideal c/a ratio as unity for the tetragonal structures AFM100 and AFM110 in order to compare their distortions (i.e. changes in the c/a ratio) to the cubic structure (see table 1). The nearest neighbor AFM ions (Ce+ and Ce−) are aligned along the c-axis and the a-axis in AFM100 and AFM110, respectively (the corresponding lattice vectors are listed in table 2). By considering the magnetic configurations and the predicted c/a ratios (>1 for AFM100 and <1 for AFM110 on the basis of both the GGA and the GGA + U), we surmise that the repulsive interaction between the AFM Ce ions (Ce+ and Ce−) is stronger than that between the FM ions (Ce+ and Ce+, or Ce− and Ce−).

The single-crystal bulk moduli, B, for the magnetic states are lower than that for the NM state since magnetic interactions expand the lattice (see the equilibrium volumes given in table 2). In addition, the bulk moduli from the GGA + U are slightly larger than those due to the GGA, indicating slightly stronger atomic interactions. The bulk modulus pressure derivative, B', which is related to the Grüneisen constant, is also related to the thermal expansion coefficient. The larger B', the larger the value of the thermal expansion coefficient [43, 63]. Table 2 gives the EOS predicted B' with values around 3.19–3.64 from both the GGA and the GGA + U. Small differences in B' suggest similar thermal expansion behavior.

5. CeMg elastic properties

Table 3 lists the GGA-predicted C_{ij} and related polycrystalline elastic moduli for each CeMg structure computed with the least-squares method [46] and from other theoretical/experimental sources. To facilitate the ensuing discussion, each entry in table 3 is labeled with a number in parenthesis listed in the first column. For AFM110, the four-atom primitive cell given in table 1 was used in the present first-principles calculations. Here the lattice vectors $\boldsymbol{a}$ and $\boldsymbol{b}$ are along [110] and [$\bar{1}$10] in the other CeMg structures (also listed in table 1), respectively, and are rotated by 45° about the c-axis. To quantitatively compare the C_{ij} computed for AFM110 with those of the other CeMg structures, we must first rotate each C_{ij} by 45° around the c-axis. The rotated elastic constants, C'_{ij}, in terms of the VASP-computed C_{ij} for AFM110 are [64, 65]

$$C'_{11} = (C_{11} + C_{12})/2 + C_{66}, \tag{2}$$

$$C'_{12} = (C_{11} + C_{12})/2 - C_{66}, \tag{3}$$

$$C'_{66} = (C_{11} - C_{12})/2, \tag{4}$$

$$C'_{13} = C_{13}, \tag{5}$$

$$C'_{33} = C_{33}, \tag{6}$$

$$C'_{44} = C_{44}. \tag{7}$$

Anisotropic cubic crystals have two unique shear moduli, namely, C_{44} and $(C_{11} - C_{12})/2$. The same is true for tetragonal crystals except for C_{66} which is a third shear modulus [25, 66]. We note that $C_{11} < C_{44}$ or $C_{11} \approx C_{44}$ (which we refer to as an elastic anomaly) is rare, occurring in the elemental (cubic) solids only for BCC Ba [26, 67]. In the specific case of Ba, this behavior signals a change from free electron-like character to a transition metal [26, 68].

Unless otherwise mentioned, the C_{ij} listed in table 3 were computed with the $5s^2 5p^6 4f 5d 6s^2$ Ce GGA-PBE potential [29]

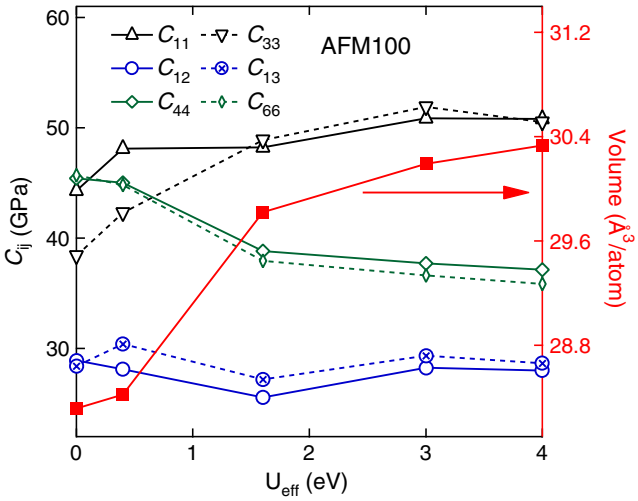

Figure 4. GGA + U-predicted equilibrium volume and elastic constants for AFM100 CeMg as a function of the effective Coulomb interaction U_{eff}.

and the equilibrium lattice parameters were predicted with this potential (see table 2). The GGA-predicted C_{ij} in entry (1) of table 3 corresponds to the NM structure. Here $C_{44} > C_{11}$ by 1.4 GPa. The C_{11} and C_{12} are close to the 110 K experimental values in entry (11) and $a \approx 3.906$ Å ($a = 3.902$ Å at 30 K and $a = 3.914$ Å at room temperature) reported in [18]. The notable exception is the shear elastic constant, C_{44}, for which that in entry (1) for 0 K exceeds the 110 K experimental value in entry (11) by 14 GPa. It is worth mentioning that the experimental C_{ij} were estimated from measured phonon spectra [18], a process that can lead to results that are inherently inaccurate, as discussed below. In addition, $C_{44} > C_{11}$ is also predicted in the present work using other exchange–correlation potentials, e.g., GGA-PW91 [22] and LDA [69, 70], when the same Ce valence ($5s^25p^64f5d6s^2$) is used. Alternative means of computing the C_{ij} also lead to the conclusion that $C_{44} > C_{11}$ on the basis of DFT theory (i.e. from both the GGA and the LDA). This is shown in entries (2) and (3) where the C_{ij} of NM CeMg were computed using the slopes of our GGA-computed zone center phonon dispersion branches and with the force constants from our phonon calculations, respectively.

Figure 4 shows the C_{ij} and equilibrium volumes of AFM100 CeMg predicted from the GGA + U as a function of U_{eff}. With increasing U_{eff}, the equilibrium volume of AFM100 increases; C_{11}, C_{33} increase; C_{12}, C_{13} remain essentially constant; and C_{44}, C_{66} decrease. When $U_{\text{eff}} >\sim 0.5$ eV, C_{11} (C_{33}) > C_{44} (C_{66}) (see also table 3); this is considered as the normal elastic behavior. But the large values of U_{eff} do not lead to a reasonable prediction of the Néel temperature ~20 K.

Entries (4)–(10) in table 3 list the C_{ij} for the magnetic CeMg structures computed with the GGA, and as an example, the C_{ij} for AFM100 from the GGA + U ($U_{\text{eff}} = 0.4$ eV and 1.6 eV) are also listed (entries (6) and (7)). Note that $C_{44} > C_{11}$ from the GGA in entries (4), (5), (9), and (10), with the FM CeMg structure showing the greatest disparity between these two moduli. The C_{11} (and C_{33}) computed with the GGA + U increase relative to the GGA results in entry (5) for AFM100, and C_{11} (C_{33}) ≈ C_{44} (C_{66}). The negative C_{12} for the AFM110 structure (entry (8)), which is based upon the lattice vectors given in table 1, suggests a negative Poisson's ratio. The C'_{ij} in entry (9) resulted from rotation of the C_{ij} in entry (8) through 45° following equations (2)–(7). In this system, $C'_{12} > 0$. In fact, equation (3) and the C_{ij} from any entry (except for entry (8)) listed in table 3 will result in $C'_{12} < 0$ in the rotated system. It is interesting to note that C_{12} and C_{13} are nearly equivalent for the AFM structures in entries (5), (6), (7) and (9). The same observation applies for C_{44} and C_{66}. This is due to the small difference between the tetragonal and cubic structures ($c/a \sim 1$; see table 2).

In summary, first-principles calculations show that the GGA-predicted C_{44} (and C_{66}) are slightly larger than C_{11} (and C_{33}) for all CeMg structures investigated with the Ce $5s^25p^64f5d6s^2$ potential. From the GGA + U, we find C_{11} (C_{33}) ≈ C_{44} (C_{66}) for $U_{\text{eff}} = 0.4$ eV, and C_{11} (C_{33}) > C_{44} (C_{66}) for large U_{eff} values (e.g. >1 eV). The latter case agrees with results estimated from phonon dispersion curves at 110 K [18] where $C_{11} > C_{44}$ by 14 GPa for the PM CeMg structure.

Also shown in table 3 are the Hill [71] polycrystalline bulk, B, and shear, G, moduli based upon our computed C_{ij}, from both the GGA and the GGA + U. The Hill moduli are a compromise between the Reuss and Voigt models which assume uniform strain and stress, respectively, in a polycrystalline material. Experiments suggest that B and G lie in between these two bounds, and Hill's proposal was an average of the Reuss and Voigt criteria [71]. The Hill moduli obtained from the C_{ij} are in close accord with the single-crystal values from the EOS fits (see table 2). The notable exception is for FM (entry (4) in table 3) where the GGA-predicted polycrystalline bulk moduli are 32.1 GPa and 28.4 GPa, respectively. The smaller bulk modulus from the EOS fit for the FM structure resulted from the fit being performed primarily on the higher volume structures (see figure 2). The computed polycrystalline bulk moduli for the cubic structures are reasonably close to that from the 110 K experiment on the PM CeMg structure [18]. From table 3, the predicted ratios, B/G, are all less than 1.75. Following the Pugh criterion which has been applied to infer ductility of numerous materials [62, 72–74], all CeMg structures have low ductility due to correspondingly low B/G ratios. According to this criterion, a 'critical' value of ~1.75 separates ductile and brittle materials.

Poisson's ratio describes volume conservation under a uniaxial stress, or the extent to which elongation in one direction causes expansion in the transverse plane [27, 75]. Table 3 lists the polycrystalline Poisson's ratios of all CeMg structures from [76],

$$\nu_{\text{poly}} = (3B_{\text{Hill}} - 2G_{\text{Hill}})/(6B_{\text{Hill}} + 2G_{\text{Hill}}). \qquad (8)$$

For all CeMg structures considered in table 3, $\nu_{\text{poly}} > 0$. However, Poisson's ratios for a single crystal may exhibit negative values along specific crystallographic directions even though $\nu_{\text{poly}} > 0$. Baughman *et al* [27] noted that 69% of the elemental cubic metals exhibit a negative Poisson's ratio

when elongated along [110]. Although thought to be rare in Nature (but not prohibited by thermodynamics), materials with negative Poisson's ratio have been the subjects of several important studies over the past two decades [27, 77, 78]. For a single crystal, a direction-dependent Poisson's ratio can be expressed as [79, 80]

$$\nu = -S'_{12}/S'_{11}. \tag{9}$$

Here, S'_{ij} is the elastic compliance in Voigt notation. The direction of longitudinal extension associated with S'_{11} is orthogonal to that of the lateral contraction associated with S'_{12}. Baughman *et al* [27] found that the minimum Poisson's ratio for a cubic symmetry results from a [110] extension measured along $[1\bar{1}0]$ or [001]. For CeMg, we found $\nu_{\min} = \nu([110], [1\bar{1}0])$ for the cubic symmetry, and $\nu_{\min} \approx \nu([110], [1\bar{1}0])$ for the tetragonal symmetry since $c/a \approx 1$ for AFM100 and AFM110 (see table 2). Therefore, $\nu_{\min} = \nu([110], [1\bar{1}0])$ was adopted for both cubic and tetragonal symmetries in the present work. For cubic symmetry, Baughman *et al* [27] gave the following expression for $\nu_{\min} = \nu([110], [1\bar{1}0])$ (based on equation (9)):

$$\nu_{\min} = -[2C_{11}C_{44} - (C_{11} - C_{12})(C_{11} + 2C_{12})]/[2C_{11}C_{44} + (C_{11} - C_{12})(C_{11} + 2C_{12})]. \tag{10}$$

Note that a version of equation (10) for the tetragonal symmetry can also be derived through equation (9). For all cubic and tetragonal CeMg structures detailed in table 3, $\nu_{\min} < 0$. Another Ce compound with a reported negative Poisson's ratio is $Ce_{0.74}Th_{0.26}$ [81]. Interestingly, Baughman *et al* [27] identified the PM 110 K CeMg structure (see entry (11) in table 3) from experiment [18] as having $\nu_{\min} < 0$, in addition to CeAg and elemental Ce. A negative Poisson's ratio, which is linked to auxetic behavior [27], is thought to be uncommon for salts having either NaCl or CsCl structures. It has been suggested that some materials exhibiting this behavior may find application as amplifiers for piezoelectric sensors [27, 76, 82].

6. Elastic properties from phonon calculations

Vibrational spectra and force constants for the interaction between ions are used to compute the elastic properties of the CeMg structures considered in section 5. The upper panel in figure 5 shows our calculated phonon dispersion relations for NM CeMg at its equilibrium volume (table 2) using the Ce ($5s^2 5p^6 4f 5d 6s^2$) PBE potential and the GGA. Experimental data from 30 and 110 K [18] are shown in figure 5 as filled circles, which are associated with transverse modes, T, and open squares, which are associated with longitudinal modes, L. Reasonable agreement between our phonon results and neutron scattering measurements is suggested. However, along the Γ–X direction (lower panel in figure 5), both the measurements and phonon calculations indicate that the frequencies of the twofold-degenerate acoustic transverse branches are very close to those of the longitudinal branch. The computed L branch from the GGA falls below that of the corresponding T branches as indicated by the arrows in the figure. The measurements

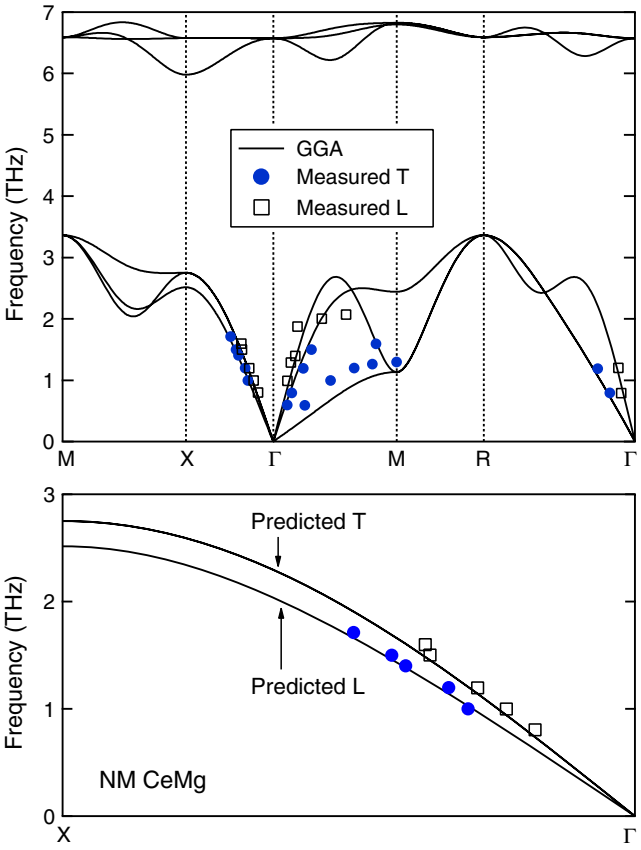

Figure 5. Phonon dispersion curves calculated using the GGA for NM CeMg together with the inelastic neutron scattering measurements (symbols) at 30 and 110 K (phonon results from experiment show no significant differences at these two temperatures) [18]. In contrast to the measurement, the present work indicates that the frequency of the longitudinal (L) acoustic branch along the Γ–X direction is lower than those of the transverse (T) acoustic branches.

suggest that the L branch falls just above the T branch (by no more than a few tenths of a terahertz) halfway along Γ–X, but otherwise the associated frequencies are nearly identical. Alternatively, the L branch from experiment falls above the T branches along Γ–M which is the expected behavior.

The C_{ij} also can be estimated using the long wave approach with phonon dispersion data. For cubic materials [83],

$$C_{11} = \rho v_1^2, \tag{11}$$

$$C_{44} = \rho v_2^2, \tag{12}$$

$$C_{11} - C_{12} = 2\rho v_3^2. \tag{13}$$

Here, ρ is the density, v_1 the wave velocity along the longitudinal ⟨100⟩ direction (i.e., the Γ–X direction), v_2 the wave velocity along the transverse ⟨100⟩ direction (Γ–X), and v_3 is the wave velocity along the slow transverse ⟨110⟩ direction (Γ–M). Velocities are defined by $v = \mathrm{d}\omega/\mathrm{d}q$ where ω is the frequency and q is the wavevector. These are obtained by a linear fitting in the lower frequency region (i.e. the long wave region) of the phonon dispersion branches. As shown in entry (2) of table 3, the GGA-predicted C_{ij} of NM

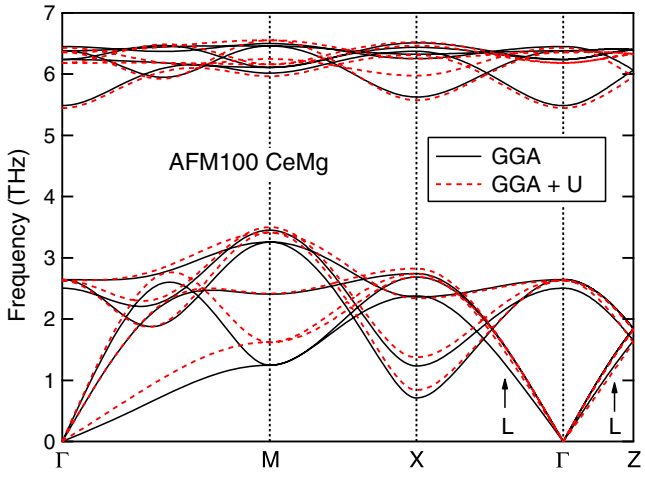

Figure 6. Phonon dispersion curves calculated using the GGA and GGA + U ($U_{\text{eff}} = 0.4$ eV) for AFM100 CeMg (see table 1 for structural details). The symbol L denotes longitudinal acoustic branches with frequencies that are lower than the corresponding transverse acoustic branches.

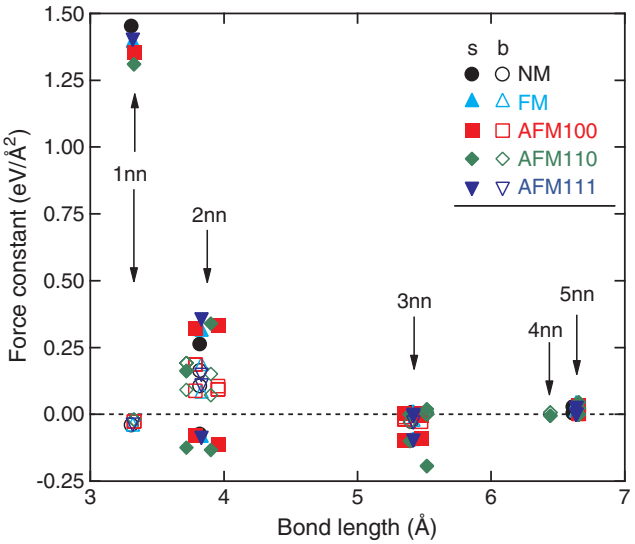

Figure 7. GGA-predicted stretching ('s', filled symbols) and bending ('b', open symbols) force constants of CeMg (see table 1 for structural details) from the first-nearest-neighbor (1nn) region up to the fifth-nearest-neighbor (5nn) region.

CeMg that result from fitting the phonon dispersion curves also show the anomalous $C_{44} > C_{11}$ relationship since acoustic T branches have slopes that exceed that of the L branch (and hence transverse vibrations propagate at speeds that exceed longitudinal vibrations). Note that the $(C_{44} - C_{11})$ predicted from the least-squares method is 1.4 GPa (GGA; see entry (1) in table 3), while the $(C_{44} - C_{11})$ from the phonon dispersion curves is 15 GPa (GGA; see entry (2) in table 3). We believe that the C_{ij} estimated from the phonon spectra are less accurate than those obtained by the other methods we have considered [84]. Our reasons are based upon the following arguments: (i) the long range interactions being ignored in the phonon calculations; (ii) the calculated forces acting on ions used to predict phonon properties being less accurate than the calculated stresses of the distorted unit cells used to compute the C_{ij} with the least-squares method. In fact, the C_{ij} estimated from measured phonon curves are also less accurate, since a small difference in wave velocity v will result in a large difference in C_{ij} since $C_{ij} \propto v^2$ (see equations (11)–(13) for the cubic case). On the basis of: (i) the least-squares method predictions (table 3); (ii) the measured phonon curves for PM CeMg (figure 5); (iii) greater inaccuracies in the C_{ij} from both measured and calculated phonon curves, we therefore assume that $C_{11} \approx C_{44}$ (C_{11} may be a few GPa larger than C_{44}) holds for each CeMg structure studied herein, especially for NM CeMg.

Figure 6 shows our phonon dispersion curves for the AFM100 structure at its equilibrium volume (see table 2) calculated from the GGA and the GGA + U. As is the case for the NM CeMg structure, phonon anomalies are also displayed in figure 6. The acoustic L branches have slopes that are less than those of the acoustic T branches in the Γ–X and Γ–Z directions, corresponding to C_{44} (C_{66}) > C_{11} (C_{33}) as given in table 3. This behavior is more pronounced in results from the GGA. The computed phonon dispersion curves of the remaining magnetic structures (FM and AFM111, not shown) lead to the same conclusions about elastic and phonon anomalies in CeMg. Note that the more accurate least-squares method with the GGA + U predicts C_{44} (C_{66}) ≈ C_{11} (C_{33}) as shown in table 3.

It is useful to analyze the force constants (FCs) obtained from our phonon calculations as a means of probing the reasons behind the result $C_{44} \approx C_{11}$ (or even $C_{44} > C_{11}$ from the GGA) for CeMg. The FCs quantify the extent of interaction or bonding between the ions. A large positive force constant suggests bonding, while a negative force constant suggests that the two ions in question would 'prefer' to move apart (but the intervening nearest neighbor ions hold them together). A zero force constant indicates that the two ions do not interact. The FCs computed from the GGA are displayed in figure 7 as a function of bond length for the five CeMg structures detailed in table 1. The stretching and bending FCs (denoted as 's' and 'b' in the figure 7 key) were calculated from the directionally dependent 3 × 3 FC matrix. Relationships between the FCs for the CeMg CsCl-type structure are given in table 4. Note that we omit the lengthy algebraic relationships for the 4nn and 5nn stretching and bending FCs. We assume that the c/a ratio of the AFM tetragonal structures is unity to facilitate the discussion. Figure 7 shows that the stretching FCs in the 1nn region (interactions between Mg and Ce) predominate. However, the bending FCs in the 1nn region are close to zero, suggesting that the components α_1 and β_1 in the FC matrix (see table 4) are nearly equivalent. Figure 7 also shows that negative stretching FCs occur for all CeMg structures in the 2nn (Mg–Mg interaction) and the 3nn regions (Ce–Ce interaction), indicating the tendency of these ions to move apart in stretching [85]. For the 4nn region (Ce–Mg bonding) shown in figure 7, the FCs are close to zero. For the 5nn region small but positive FCs correspond to Ce–Ce interactions (those closest to zero correspond to the Mg–Mg case). The stretching and bending FCs in the 2nn and the 3nn regions in the GGA

Table 4. Force constant (FC) matrices and expressions for stretching (s) and bending (b) FCs for the first-, the second-, and the third-nearest neighbors (nn) of the CsCl-type structure.

	Fractional coordinates			
nn	Site A	Site B	FC matrix	Stretching and bending FC
1nn	(0, 0, 0)	(1/2, 1/2, 1/2)	$\begin{pmatrix} \alpha_1 & \beta_1 & \beta_1 \\ \beta_1 & \alpha_1 & \beta_1 \\ \beta_1 & \beta_1 & \alpha_1 \end{pmatrix}$	$FC_1(s) = \alpha_1 + 2\beta_1$ $FC_1(b) = \alpha_1 - \beta_1$
2nn	(0, 0, 0)	(0, 0, 1)	$\begin{pmatrix} \beta_2 & 0 & 0 \\ 0 & \beta_2 & 0 \\ 0 & 0 & \alpha_2 \end{pmatrix}$	$FC_2(s) = \alpha_2$ $FC_2(b) = \beta_2$
3nn	(0, 0, 0)	(0, 1, 1)	$\begin{pmatrix} \alpha_3 & 0 & 0 \\ 0 & \beta_3 & \gamma_3 \\ 0 & \gamma_3 & \beta_3 \end{pmatrix}$	$FC_3(s) = \beta_3 + \gamma_3$ $FC_3(b) = (\alpha_3 + \beta_3 - \gamma_3)/2$

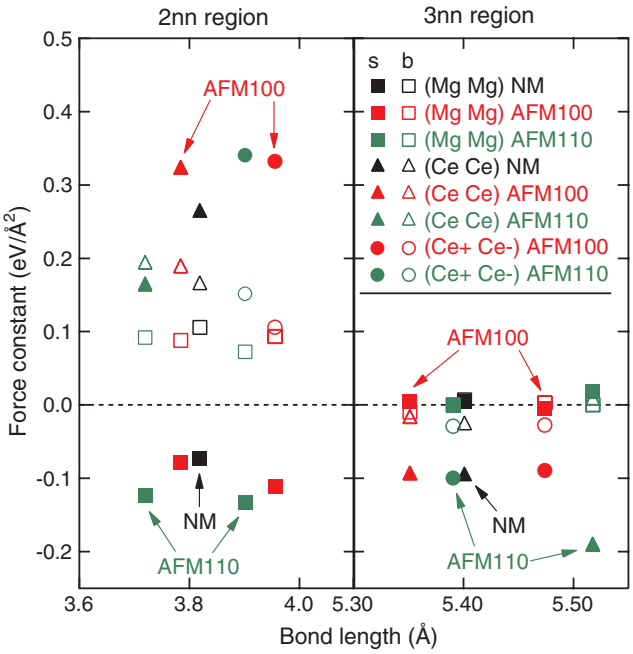

Figure 8. GGA-predicted stretching ('s', filled symbols) and bending ('b', open symbols) force constants of NM, AFM100 and AFM110 CeMg (see table 1 for structural details) in the second-nearest-neighbor (2nn) and the third-nearest-neighbor (3nn) regions.

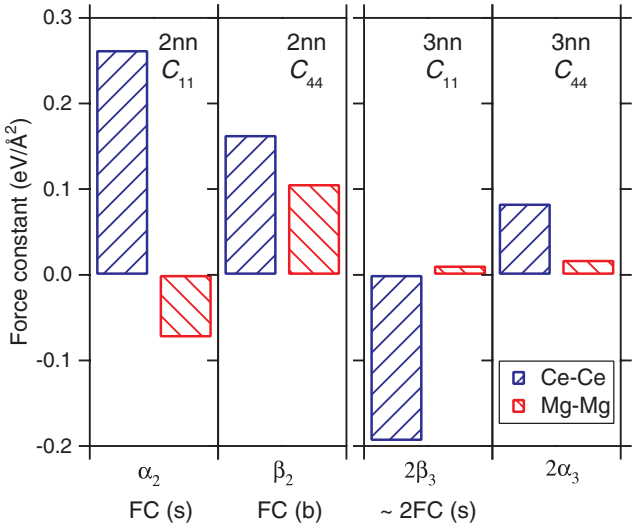

Figure 9. Contributions of force constants (FCs) from the second- and the third-nearest neighbors (2nn and 3nn) of NM CeMg (see table 4 and equations (14) and (15)) predicted from the GGA. The negative stretching FC for the 2nn Mg–Mg and the 3nn Ce–Ce interactions are responsible for $C_{11} < C_{44}$.

are shown in greater detail in figure 8 for NM, AFM100, and AFM110. Note that the FCs obtained from the GGA + U (not shown) lead to similar conclusions, as indicated by the similarities of C_{ij} predicted from the GGA and the GGA + U (see table 3).

The C_{ij} can also be estimated from the FCs. For instance, the following relationships apply for the NM CeMg CsCl-type structure up to the 3nn [86]:

$$C_{11} = \sum_{n=A,B} [\alpha_1^{A-B} + \alpha_2^{n-n} + 4\beta_3^{n-n}]/a_0, \quad (14)$$

$$C_{44} = \sum_{n=A,B} [\alpha_1^{A-B} + \beta_2^{n-n} + (2\alpha_3^{n-n} + 2\beta_3^{n-n})]/a_0, \quad (15)$$

$$C_{12} = \sum_{n=A,B} [(2\beta_1^{A-B} - \alpha_1^{A-B}) - \beta_2^{n-n} + (4\gamma_3 - 2\alpha_3^{n-n} - 2\beta_3^{n-n})]/a_0, \quad (16)$$

where a_0 is the equilibrium lattice parameter, A and B represent distinct ionic sites, the superscript 'n–n' pertains to 'A–A' or 'B–B', and remaining symbols are detailed in table 4. Equations (14)–(16) show that the 1nn FCs have the same contribution to C_{11} and C_{44}. The difference between C_{11} and C_{44} is due to the 2nn and the 3nn interactions as indicated by equations (14) and (15). For example, the FC components in the 2nn and the 3nn regions (α_2, β_2, $2\alpha_3$, and $2\beta_3$) which lead to the difference between C_{11} and C_{44}, are shown in figure 9 for NM CeMg from the GGA. Clearly, the negative FC contributions have more of an impact on C_{11} than on C_{44}. As shown in figure 9, the negative contribution of the FC in the 2nn region (α_2 or stretching FC; see equations (14)–(16) and table 4) is due to the interaction between Mg ions. The negative FC in the 3nn region (2 β_3 or stretching FC due to γ_3 in table 4 being close to zero) is caused by the Ce–Ce ion interaction as shown in figure 9. The C_{ij} calculated from the FCs (up to the 5nn) are listed in table 3 for NM CeMg (entry (3) from the GGA). These are close to those from the relations between the sound speeds in equations (11)–(13) (entry (2)).

In fact, these conclusions for NM CeMg from figure 9 and equations (11)–(13) also hold for the other CeMg structures, as indicated by the similarities between the associated stretching and bending FCs in figures 7 and 8. Therefore, the origin of the anomalous $C_{44} \approx C_{11}$ (or $C_{44} > C_{11}$ in the GGA) for CeMg is primarily the negative stretching FCs for the 2nn Mg–Mg ion interaction and especially the 3nn Ce–Ce ion interaction. Furthermore, figure 9 shows that (i) the positive Ce–Ce FCs in the 2nn region (i.e., for the nearest Ce–Ce ions), and (ii) the FCs for the interaction between the FM Ce ions (Ce+ versus Ce+ or Ce− versus Ce−) are less than those for the interaction between the AFM Ce ions (Ce+ versus Ce−). This indicates that interactions between the AFM Ce atoms are larger than those that are not antiferromagnetic, and $c/a > 1$ will result for AFM100 and $c/a < 1$ for AFM110, as predicted (see table 2).

7. Conclusions

Phase stability due to magnetism together with elastic and phonon properties of the CsCl-type heavy fermion compound CeMg (1:1 Ce:Mg) were investigated with the implementation of plane wave density functional theory in the VASP code. In contrast to the case for a previous first-principles study of CeMg where a core state model of Ce f electrons was used, all calculations in the present study employed a Ce PAW potential with Ce f electrons in the valence. Results from the GGA and the GGA + U, which accounts for strong correlation in localized Ce 4f electrons with an effective Coulomb interaction, U_{eff}, were compared. We found that $U_{\text{eff}} = 0.4$ eV leads to accurate prediction of the CeMg ground state (AFM100) and leads to an estimated Néel temperature that is very close to the 20 K value from experiment. The GGA leads to a low energy CeMg structure that is also an AFM state but with wavevector along [110]: this disagrees with experiment. Using a least-squares fitting method, we computed the C_{ij} of each of five CeMg structures. For each structure, $C_{44} \approx C_{11}$ for small U_{eff} values, e.g. <1 eV (or $C_{44} > C_{11}$ mainly from the GGA), which suggests an elastic anomaly associated with the transverse sound speeds equaling (or exceeding) the longitudinal sound speed. This behavior was supported with computed phonon dispersion relations based upon the direct method for lattice dynamics, especially in the GGA. The predicted frequencies of the longitudinal acoustic branch along the Γ–X direction are lower than those of the transverse branches. The origin of this behavior is associated with negative stretching force constants for the second-nearest-neighbor Mg–Mg ion interaction and especially the third-nearest-neighbor Ce–Ce ion interaction. Polycrystalline values of Poisson's ratio based upon the Hill criterion range between 0.19 and 0.28. However, for all CeMg structures, we find negative Poisson's ratio values (from −0.30 to −0.74) due to an elongation along [110] measured in $[1\bar{1}0]$.

Acknowledgments

The authors greatly benefited from the very helpful advice of Professor J Hafner, E Wimmer, P Saxe, and R Windiks. This work was funded by the National Science Foundation (NSF) through Grants Nos DMR-0510180 and DMR-0205232. First-principles calculations were carried out at the General Motors High Performance Computing Center on p6-575 IBM clusters and the Cobalt system at NCSA supported by NSF through TeraGrid resources under Grant No. DMR-080032N.

References

[1] Mathur N D, Grosche F M, Julian S R, Walker I R, Freye D M, Haselwimmer R K W and Lonzarich G G 1998 *Nature* **394** 39–43
[2] Barbara B and Zemirli S 1988 *J. Physique* **49** 789–90
[3] Pierre J, Galera R M and Siaud E 1985 *J. Physique* **46** 621–6
[4] Beille J, Najib A, Galera R M and Pierre J 1987 *J. Magn. Magn. Mater.* **63–4** 111–3
[5] Nakawaki H *et al* 2002 *J. Phys.: Condens. Matter* **14** L305–11
[6] Hegger H, Petrovic C, Moshopoulou E G, Hundley M F, Sarrao J L, Fisk Z and Thompson J D 2000 *Phys. Rev. Lett.* **84** 4986–9
[7] Rokhlin L L 2003 *Magnesium Alloys Containing Rare Earth Metals: Structure and Properties* (London: Taylor and Francis)
[8] Mordike B L 2001 *J. Mater. Process. Technol.* **117** 391–4
[9] Pekguleryuz M O *et al* 2002 *J. Met.* **54** 18–21
[10] Shepeleva L and Bamberger M 2006 *Mater. Sci. Eng.* A **425** 312–7
[11] Smola B, Stulikova I, von Buch F and Mordike B L 2002 *Mater. Sci. Eng.* A **324** 113–7
[12] Wang T, Zhang M L, Niu Z Y and Liu B 2006 *J. Rare Earths* **24** 797–800
[13] Wu W H and Xia C Q 2004 *J. Cent. South Univ. Technol.* **11** 367–70
[14] Mishra R K, Gupta A K, Rao P R, Sachdev A K, Kumar A M and Luo A A 2008 *GM Research Publication R&D* 10926
[15] Villars P and Calvert L D 1991 *Pearson's Handbook of Crystallographic Data for Intermetallic Phases* 2nd edn (Newbury, OH: ASTM International)
[16] Galera R M, Pierre J, Voiron J and Dampne G 1983 *Solid State Commun.* **46** 45–6
[17] Schmitt D, Morin P and Pierre J 1978 *J. Magn. Magn. Mater.* **8** 249–56
[18] Pierre J, Galera R M and Bouillot J 1984 *J. Magn. Magn. Mater.* **42** 139–47
[19] Kresse G and Furthmuller J 1996 *Comput. Mater. Sci.* **6** 15–50
[20] Kresse G and Furthmuller J 1996 *Phys. Rev.* B **54** 11169–86
[21] Wu Y and Hu W 2007 *Eur. Phys. J.* B **60** 75–81
[22] Perdew J P, Chevary J A, Vosko S H, Jackson K A, Pederson M R, Singh D J and Fiolhais C 1992 *Phys. Rev.* B **46** 6671–87
[23] Kresse G and Joubert D 1999 *Phys. Rev.* B **59** 1758–75
[24] Thalmeier P 1987 *J. Phys. C: Solid State Phys.* **20** 4449–66
[25] Shukla M M 1982 *J. Phys. D: Appl. Phys.* **15** L177–80
[26] Mizuki J, Chen Y, Ho K M and Stassis C 1985 *Phys. Rev.* B **32** 666–70
[27] Baughman R H, Shacklette J M, Zakhidov A A and Stafstrom S 1998 *Nature* **392** 362–5
[28] Haule K, Oudovenko V, Savrasov S Y and Kotliar G 2005 *Phys. Rev. Lett.* **94** 036401
[29] Perdew J P, Burke K and Ernzerhof M 1996 *Phys. Rev. Lett.* **77** 3865–8
[30] Vosko S H, Wilk L and Nusair M 1980 *Can. J. Phys.* **58** 1200–11
[31] Dudarev S L, Botton G A, Savrasov S Y, Humphreys C J and Sutton A P 1998 *Phys. Rev.* B **57** 1505–9
[32] Hafner J 2008 *J. Comput. Chem.* **29** 2044–78
[33] Cococcioni M and de Gironcoli S 2005 *Phys. Rev.* B **71** 035105

[34] Fabris S, de Gironcoli S, Baroni S, Vicario G and Balducci G 2005 *Phys. Rev.* B **71** 041102
[35] Andersson D A, Simak S I, Johansson B, Abrikosov I A and Skorodumova N V 2007 *Phys. Rev.* B **75** 035109
[36] Loschen C, Carrasco J, Neyman K M and Illas F 2007 *Phys. Rev.* B **75** 035115
[37] Windiks R, Winimer E, Pourovskii L, Biermann S and Georges A 2008 *J. Alloys Compounds* **459** 438–46
[38] Rohrbach A, Hafner J and Kresse G 2004 *Phys. Rev.* B **69** 075413
[39] Zhou F, Cococcioni M, Marianetti C A, Morgan D and Ceder G 2004 *Phys. Rev.* B **70** 235121
[40] Shukla N N, Shukla S, Prasad R and Benedek R 2008 *Model. Simul. Mater. Sci. Eng.* **16** 055008
[41] Ciucivara A, Sahu B and Kleinman L 2008 *Phys. Rev.* B **77** 092407
[42] Gupta F, Brillant G and Pasturel A 2007 *Phil. Mag.* **87** 2561–9
[43] Shang S and Böttger A 2005 *Acta Mater.* **53** 255–64
[44] Monkhorst H J and Pack J D 1976 *Phys. Rev.* B **13** 5188–92
[45] Blöchl P E, Jepsen O and Andersen O K 1994 *Phys. Rev.* B **49** 16223–33
[46] Le Page Y and Saxe P 2002 *Phys. Rev.* B **65** 104104
[47] Gressmann T, Wohlschlogel M, Shang S, Welzel U, Leineweber A, Mittemeijer E J and Liu Z K 2007 *Acta Mater.* **55** 5833–43
[48] Gladden J R, So J H, Maynard J D, Saxe P W and Le Page Y 2004 *Appl. Phys. Lett.* **85** 392–4
[49] Minisini B, El Hadj L, Fomena M L, Van Garderen N and Tsobnang F 2006 *J. Phys.: Condens. Matter* **18** 2429–41
[50] Hector L G Jr, Herbst J F, Wolf W, Saxe P and Kresse G 2007 *Phys. Rev.* B **76** 014121
[51] Shang S L, Wang Y and Liu Z K 2007 *Appl. Phys. Lett.* **90** 101909
[52] Woodward C, Trinkle D R, Hector L G Jr and Olmsted D L 2008 *Phys. Rev. Lett.* **100** 045507
[53] Wrobel J and Piechota J 2008 *Solid State Commun.* **146** 324–9
[54] Parlinski K, Li Z Q and Kawazoe Y 1997 *Phys. Rev. Lett.* **78** 4063–6
[55] van de Walle A and Ceder G 2002 *Rev. Mod. Phys.* **74** 11–45
[56] Parlinski K 2005 *Software Phonon, as Implemented in MedeA 2.2* (Angel Fire, NM: Materials Design)
[57] Methfessel M and Paxton A T 1989 *Phys. Rev.* B **40** 3616–21
[58] Hector L G Jr and Herbst J F 2008 *J. Phys.: Condens. Matter* **20** 064229
[59] Wang Y, Hector L G Jr, Zhang H, Shang S L, Chen L Q and Liu Z K 2008 *Phys. Rev.* B **78** 104113
[60] Cococcioni M 2002 A LDA + U study of selected iron compounds *PhD Thesis* Trieste, Italy: International School for Advanced Studies
[61] Yang I, Savrasov S Y and Kotliar G 2001 *Phys. Rev. Lett.* **87** 216405
[62] Hector L G Jr and Herbst J F 2004 *J. Alloys Compounds* **379** 41–53
[63] Shang S L, Bottger A J and Liu Z K 2008 *Acta Mater.* **56** 719–25
[64] Nye J F 1985 *Physical Properties of Crystals: Their Representation by Tensors and Matrices* (Oxford: Oxford University Press)
[65] Ting T C T 2000 *Q. J. Mech. Appl. Math.* **53** 511–23
[66] Grimvall G 1999 *Thermophysical Properties of Matter* (New York: Elsevier) at press
[67] Every A G, McCurdy A K and Nelson D F (ed) 1992 *Second and Higher Order Elastic Constants* (*Landolt–Börnstein New Series* Group III, vol 29a) (Berlin: Springer) p 11
[68] Shang S L, Wang Y and Liu Z K 2007 *Phys. Rev.* B **75** 024302
[69] Ceperley D M and Alder B J 1980 *Phys. Rev. Lett.* **45** 566–9
[70] Perdew J P and Zunger A 1981 *Phys. Rev.* B **23** 5048–79
[71] Hill R 1952 *Proc. Phys. Soc. London* A **65** 349–55
[72] Pugh S F 1954 *Phil. Mag.* **45** 823–43
[73] Vitos L, Korzhavyi P A and Johansson B 2003 *Nat. Mater.* **2** 25–8
[74] Morris J R, Ye Y Y, Lee Y B, Harmon B N, Gschneidner K A and Russell A M 2004 *Acta Mater.* **52** 4849–57
[75] Mendik M and Wachter P 1993 *Physica* B **190** 72–3
[76] Yeganehhaeri A, Weidner D J and Parise J B 1992 *Science* **257** 650–2
[77] Rothenburg L, Berlin A A and Bathurst R J 1991 *Nature* **354** 470–2
[78] Keskar N R and Chelikowsky J R 1992 *Nature* **358** 222–4
[79] Ting T C T 2005 *J. Elast.* **81** 271–92
[80] Ting T C T and Barnett D M 2005 *Trans. ASME, J. Appl. Mech.* **72** 929–31
[81] Lüthi B 2007 *Physical Acoustics in the Solid State* (Berlin: Springer)
[82] Lakes R 1993 *Adv. Mater.* **5** 293–6
[83] Barker J A, Klein M L and Bobetic M V 1970 *Phys. Rev.* B **2** 4176–9
[84] Jochym P T, Parlinski K and Sternik M 1999 *Eur. Phys. J.* B **10** 9–13
[85] Shirai K 1997 *J. Solid State Chem.* **133** 327–34
[86] MacDonald R A 1972 *Phys. Rev.* B **5** 4139–43